Additive Manufacturing Letters 14 (2025) 100299

Contents lists available at ScienceDirect

Additive Manufacturing Letters

journal homepage: www.elsevier.com/locate/addlet

Short communication

Chamfer distance for non-linear registration of Triply Periodic Minimal Surface lattices

Michela Lapenna [a,*], Francesco Faglioni [b], Keerthana Chand [c], Bardia Hejazi [c], Rita Fioresi [d], Giovanni Bruno [c,e]

[a] DIFA, University of Bologna (Unibo), Via Irnerio 46, Bologna, 40126, Italy
[b] DGSC, University of Modena and Reggio Emilia (Unimore), Via Campi 103, Modena, 41100, Italy
[c] Bundesanstalt für Materialforschung und -prüfung (BAM), Unter den Eichen 87, Berlin, 12205, Germany
[d] Fabit, University of Bologna (Unibo), Via San Donato 15, Bologna, 40127, Italy
[e] Institute of Physics and Astronomy, University of Potsdam, Karl-Liebknecht-Straße 24/25, Potsdam, 14476, Germany

ARTICLE INFO

Keywords:
Non-linear registration
Additive manufacturing
Computed tomography
Triple periodic minimal surface

ABSTRACT

We present a 3D image registration technique for non-linear deformation estimation in Additive Manufacturing processes. The methodology involves comparing X-ray Computed Tomography (XCT) data with Computer Aided Design (CAD) models for Triply Periodic Minimal Surface (TPMS) lattices and employs the Chamfer distance to refine mesh non-linear deformations.

1. Introduction

Image registration is crucial for quantifying deformations due to the Additive Manufacturing (AM) process. The goal is to compare the actual volume, for instance extracted via X-ray Computed Tomography (XCT) data, with the nominal volume (CAD data), while addressing global and local transformations. Several studies in AM processes have explored registration techniques to enhance accuracy and reliability [1–4].

Usually, the registration problem is solved in two steps: linear and non-linear transformation. The linear displacements, such as global translation and rotation, are primarily caused by factors like differences in sensor and coordinate systems (e.g., resolution, perspective view, etc.). These displacements can be considered as rigid body transformations, where the overall shape of the object remains unchanged, and only its position or orientation is adjusted. Linear displacements are typically easier to model, often requiring simple mathematical operations, such as translation and rotation matrices.

Non-linear displacements are more complex and are primarily associated with shape deformations such as local distortion, local shrinkage, or local stretching. These displacements reflect the actual changes in the object's shape due to external factors (e.g., loads, temperature gradients etc.) and their magnitude can vary significantly across the sample. Non-linear displacements often require more advanced computational techniques, such as iterative optimization methods, to find the best fit between the original and deformed structures. For this reason, non-linear transformations are often computationally expensive, which increases the complexity and time required for a successful registration.

A key challenge in registration, therefore, is in effectively separating these linear and non-linear components of the total deformation. Even if linear registration is usually faster and simpler with respect to the non-linear one, we stress that both linear and non-linear registration are very sensitive to the resolution of the data and the accuracy of the initial alignment. Furthermore, effectively separating alignment quality and non linear effects is still an unsolved problem [1].

In recent years, deep learning-based registration methods, such as VoxelMorph [5], AiR [6], NICE-Net [7], and deep implicit optimization approaches [8], have gained attention for their ability to perform accurate registration. Deep learning algorithms can generalize well across different datasets and learn complex deformation patterns from large amounts of training data. However, traditional methods remain widely used due to their interpretability, adaptability, and robustness in cases where data availability is limited. One example, which we employ in the present work, consists in using the Chamfer distance [9] to directly minimize the point-to-point distance between two shapes. This enables precise geometric alignment via direct mathematical minimization, without relying on learned latent patterns to guide the registration process, as typical in deep learning approaches. We emphasize that, due to its simplicity and efficiency, Chamfer distance has been widely employed by the deep learning community as well

* Corresponding author.
E-mail addresses: michela.lapenna4@unibo.it (M. Lapenna), francesco.faglioni@unimore.it (F. Faglioni), keerthana.chand@bam.de (K. Chand), bardia.hejazi@bam.de (B. Hejazi), rita.fioresi@unibo.it (R. Fioresi), giovanni.bruno@bam.de (G. Bruno).

https://doi.org/10.1016/j.addlet.2025.100299
Received 17 April 2025; Received in revised form 23 June 2025; Accepted 2 July 2025
Available online 14 July 2025

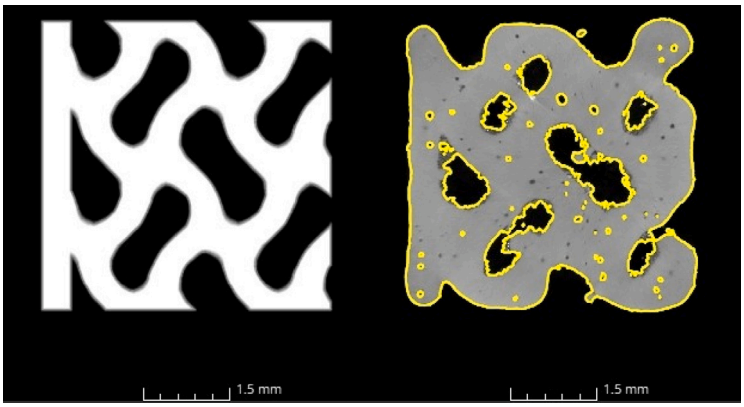

Fig. 1. Example of CAD (left) and XCT (right) 2D slices, taken perpendicular to the building direction. The yellow boundary in the right image highlights the effect of surface determination in VGStudio Max software before segmentation of the XCT volume.

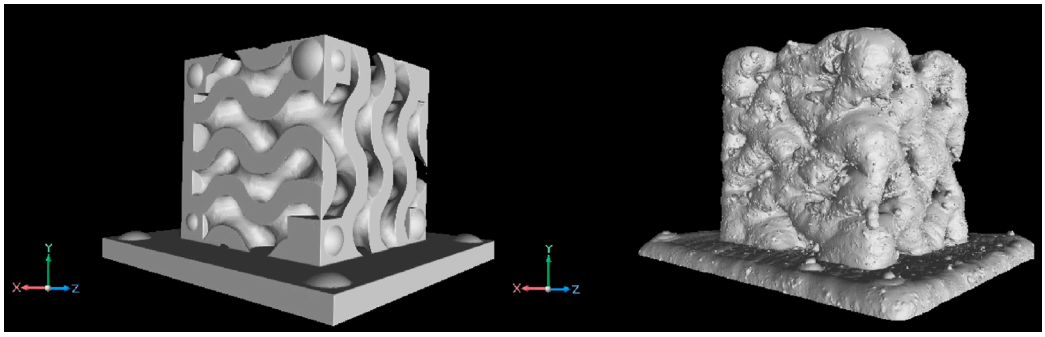

Fig. 2. CAD (left) and XCT (right) raw volumes before non-linear registration. The two volumes in the figure were linearly registered through feature-based registration exploiting the spheres on the CAD volume.

as a similarity evaluation protocol for point clouds reconstruction and registration [10–14]. Among other traditional methods, we cite the Thin-Plate Splines [15] and the B-Spline Free-Form Deformations [16] models, commonly employed in medical image registration.

With respect to deep learning methods, traditional approaches require fewer computational resources, and do not rely on extensive training data. Also, non-deep learning models allow full control over the registration process, including the ability to quantify and manage errors, whereas deep learning models often function as a black box, making it more challenging to interpret and diagnose errors. The choice between deep learning and traditional techniques ultimately depends on the application requirements, computational constraints, and the nature of the deformation being modeled.

In the present work we employ the Chamfer distance as a loss function to solve a non-linear registration task on a single Triply Periodic Minimal Surface (TPMS) mesh. To the best of our knowledge, we are not aware of other studies that show the advantages of a Chamfer distance-based non-linear registration method in this specific context within the AM domain.

2. Data and preprocessing

In this study, we analyzed Triply Periodic Minimal Surface (TPMS) lattices [17], which are widely used in several industries because of their high surface area and mechanical efficiency. Due to their complexity, such structures can be basically only manufactured via AM methods, in particular Powder Bed Fusion–Laser Beam (PBF-LB). These structures exhibit unique geometric configurations that enhance key mechanical properties, such as strength-to-weight ratio and energy absorption, making them ideal for various industrial applications involving porous materials (typically heat exchangers are now made with them, but TPMS find their way also as implants for bone reconstruction) [17–21].

2.1. Data description

The dataset we used consist of reconstructions of XCT data and of the corresponding CAD models (used for the PBF-LB fabrication process) for seven TPMS volumes, see Fig. 1 for a 2D slice and Fig. 2 for the 3D volume. The minimal surface for the TPMS volumes is governed by the following equation (see [22,23] for a theoretical analysis of TPMS geometry):

$$\cos(\lambda_x x)\sin(\lambda_y y) + \cos(\lambda_y y)\sin(\lambda_z z) + \cos(\lambda_z z)\sin(\lambda_x x) = C \tag{1}$$

In this equation, λ_x, λ_y, and λ_z control the periodicity of the pattern, and C is the level set parameter that governs the position of the boundary surface between the void and solid material. For $C = 0$, the fundamental symmetric shape is obtained. The parameter C directly influences the morphology of the TPMS. We stress however that in the present work we focused on one volume, corresponding to $C = -0.1$.

The periodicity of the surface is also controlled by the λ values, which are referred to as the dilation factors. These factors depend on the number of unit cells and the size of the unit cell in the structure, which are the parameters fixed in Siemens NX 2406 software to generate the TPMS structures. This level-set approximation technique was used to model the TPMS, where the equation represents the implicit surface, while the boundary surface is defined by the value of C.

The TPMS volume is composed of an Aluminum alloy (AlSi10Mg) and has dimension of 125 mm^3. The TPMS structures were imaged using the diondo dXmax X-ray computed tomography machine at the X-ray Imaging department of BAM. The X-ray tube was operated at a voltage of 60 kV and a current of 167 μA. The total number of projections was 3900 with a detector exposure time per projection of 1.8 s. The samples were placed at a focus-object-distance (FOD) of 28.77 mm and a focus-detector-distance (FDD) of 800 mm. The XCT scan nominal voxel size calculated by the machine software was 10 μm. Each projection had a

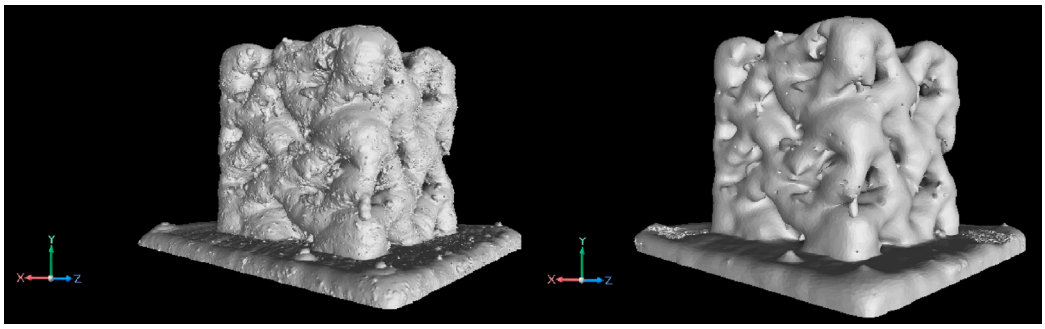

Fig. 3. XCT volume before (left) and after (right) surface smoothing. The XCT mesh was smoothed to reduce surface roughness and eliminate excess material within the voids of the periodic structure.

size of 3000 × 3000 pixels. Low-energy photons were filtered to reduce beam hardening artifacts by using a 1 mm Aluminum filter for the X-ray beam.

2.2. Linear registration and preprocessing

Prior to this work, the XCT volume was segmented using the advanced surface determination algorithm available in VGStudio Max software (Volume Graphics, Heidelberg Germany), a tool developed by Volume Graphics for the analysis and visualization of XCT data, see Fig. 1. The purpose of the segmentation was to binarize the gray levels between void and material.

Then, to correct global misalignment before applying non-linear adjustments, the CAD and XCT data were first registered through a linear transformation. Specifically, surface points were fitted to spheres located on the CAD volume, see Fig. 2. The centers of these fitted spheres were extracted, and a least squares error fit was applied to achieve accurate alignment. Spheres were chosen due to their superior radiographic contrast and minimal form deviation [24,25]. Moreover, the accuracy in determining a sphere's center is significantly higher compared to other geometric features in XCT, such as planes. This is because the symmetry of a sphere ensures that errors are uniformly distributed across its surface, resulting in a more precise center estimation [25].

After linear registration, we constructed a mesh on both the CAD and the linearly registered XCT volumes. A mesh is a collection of vertices, edges, and faces that define the shape of a 3D object, typically used for surface representation and analysis [26–28]. In this process, the mesh was generated using VGStudio Max software, ensuring an accurate and high-resolution representation of the XCT data for further comparison with the CAD model. We highlight that recent research has increasingly favored mesh-based surface registration as a strategy for XCT-to-CAD alignment [1,4].

The XCT mesh was subsequently smoothed to reduce surface roughness and eliminate excess material within the voids of the periodic structure; see Fig. 3 for a comparison between smoothed and non-smoothed XCT volumes. The initial mesh files were processed using Ansys SpaceClaim, following an iterative approach. First, the number of mesh triangles was reduced by 75%, after which the Auto Fix function was applied to correct any defects in the reduced mesh. This denoised the surface and removed the roughness by just deleting points while keeping the overall structure. Any small, disconnected elements were then identified and removed. The 75% reduction in the number of mesh triangles was achieved through two consecutive 50% reductions. This stepwise approach was deliberately chosen to maintain the overall geometry and structural integrity of the component. A single, more aggressive, reduction could result in the loss of critical details. The smoothing process continued with the Smooth tool, using the Add Facets option with a 60 degree angle threshold. This value was chosen because it is the default setting in the software and has consistently produced reliable results in preserving important geometrical features while smoothing sharp angles. This option allowed vertex positions to move and possibly increased the number of triangles while smoothing the mesh. The angle threshold ensured that sharp edges where faces meet at angles above the specified limit remained unmodified. To further smooth the mesh, the Volume Aware option was used with the same 60 degree angle threshold. This option maintained the total triangle count while preserving the overall volume of the structure. The entire process was repeated once more to obtain the final smoothed mesh.

We stress that internal process-induced defects, such as lack-of-fusion pores or keyholes, may introduce local irregularities that compromise the accuracy of surface registration. To mitigate these effects, isolated components such as pores and powder particles trapped within the TPMS structure were removed during the segmentation and mesh extraction steps. In addition, the smoothing procedure not only reduces surface roughness and excess material but also helps to eliminate residual small, disconnected elements, thereby refining the overall mesh geometry. It should be noted, however, that volumetric defects (e.g., pores or cracks) are not explicitly included in our study, which only deals with surface registration.

3. Method

The Chamfer distance was used to measure the similarity between the source (XCT) and the target (CAD) meshes, serving as the loss function for non-linear registration. Formally, the Chamfer distance loss is defined as:

$$\mathcal{L}_{\text{Chamfer}}(S,T) = \sum_{s\in S} \min_{t\in T} \|s-t\|^2 + \sum_{t\in T} \min_{s\in S} \|t-s\|^2, \tag{2}$$

where S and T are the point sets representing the vertices of the source and target meshes, respectively, and $\|s-t\|$ is the Euclidean distance between points s and t. The total number of vertices in both the CAD and the smoothed XCT meshes is approximately 100,000, while the number of triangles is around 200,000. Importantly, S and T do not necessarily have the same number of points, meaning there is no direct one-to-one correspondence between their vertices. The loss function computes the sum of distances from each point in S to its nearest neighbor in T, plus the sum of distances from each point in T to its nearest neighbor in S. This was done iteratively to progressively refine the displacement field. In this context, the displacement field represents the set of displacement vectors applied to each vertex in the source mesh to achieve alignment with the target mesh. It is a tensor of shape $(N,3)$, where N is the number of vertices in the source mesh, and each row corresponds to a displacement vector (x,y,z) for a vertex.

Initially, the displacement field was set to zero. Then, at each iteration, the displacement field was updated, gradually adjusting the position of each vertex in the source mesh to minimize the Chamfer distance with respect to the target mesh. Importantly, this process involved no direct correspondence between points on the source and

target meshes, as the nearest neighbor can change at each iteration. The final output consists of a refined displacement field that aligns the source mesh with the target mesh.

The optimization was carried out using stochastic gradient descent (SGD) [29] with momentum set to 0.9 and a learning rate of 1.0, running for $N_{\text{iter}} = 100{,}000$ iterations. Several shape regularization terms were incorporated into the objective to enforce smoothness, with a specific weight for each term. The total loss was then:

$$\mathcal{L}_{\text{total}} = 1.0 \cdot \mathcal{L}_{\text{Chamfer}} + 1.0 \cdot \mathcal{L}_{\text{edge}} + 0.01 \cdot \mathcal{L}_{\text{normal}} + 0.1 \cdot \mathcal{L}_{\text{laplacian}}, \quad (3)$$

where $\mathcal{L}_{\text{edge}}$ minimizes the length of the edges in the predicted mesh, $\mathcal{L}_{\text{nomal}}$ enforces consistency across the normals of neighboring faces and $\mathcal{L}_{\text{laplacian}}$ is the laplacian regularizer. The code to implement the total loss is directly available in Pytorch3D [30]. These regularization terms helped in maintaining geometric integrity and preventing unwanted distortions during the registration process. One of the main advantages of the Chamfer distance approach is its efficiency: directly operating on meshes, as opposed to voxel-based methods, is more memory-efficient and scalable for large-scale 3D registration tasks. Indeed, the number of vertices in a mesh is typically much lower than the number of voxels in the original volume. This is because meshes only encode the surface geometry, while typical high-resolution 3D XCT scans store values for every small unit of volume, regardless of whether it is part of the actual object or empty space. As a result, the non-linear registration of a single volume was completed in just three hours when using a GPU (NVIDIA GeForce RTX 3090 Ti, 24 GB VRAM).

The scalability of the method is primarily influenced by the complexity of the mesh required to accurately represent the surface geometry. Since the registration operates on surface meshes extracted from the XCT volume, the number of mesh vertices depends on the level of surface detail needed. For smoother or less complex geometries, a coarse mesh may suffice, even at high voxel resolutions. In contrast, for more intricate geometries, a higher voxel resolution can facilitate the extraction of finer meshes with a greater number of vertices, which in turn increases processing time. The Chamfer distance loss itself scales linearly with the number of points, as it computes the distance from each vertex in the source mesh to its nearest neighbor in the target mesh, and vice versa. This ensures that the method remains computationally efficient even for large and complex components. Furthermore, while the presented results focus on a specific TPMS structure, we expect the proposed approach to be relevant for different AM geometries with minor adjustments, such as adjusting the mesh granularity to the size and shape of interest or, possibly, decomposing registration displacements into components parallel and perpendicular to the surface at each point, making it suitable for broader industrial applications.

4. Visualization of registration effects

In Fig. 4, we present visual comparisons of the CAD and XCT meshes registered with respect to one another. These 2D visualizations illustrate the alignment improvements after non-linear registration. Specifically, we notice how the registration sometimes fails when the periodic voids of the TPMS structure are split into two smaller components, likely due to manufacturing defects that distort the designed geometry. While the registration algorithm is generally robust and does not fail in all such cases, its performance is ultimately constrained by the quality of the input data and cannot fully compensate for severe deviations from the designed geometry. In Fig. 5, we show the 3D raw volume comparison.

To further analyze the effects of registration, we visualized the normal displacement vector for each mesh vertex in 3D, see Fig. 6. Since the mesh was saved with micrometer (μm) coordinates, all displacement values are expressed in micrometers. The normal displacement vector was computed by projecting the overall displacement vector onto the surface normal using VTK (Visualization Toolkit for 3D rendering).

This enabled a pointwise analysis of how each vertex on the original XCT mesh moved as a result of the non-linear registration process to the CAD. As shown in the heatmap in Fig. 6, the AM process induced an overall significant outward displacement along the vertical y-axis, as well as along a preferred direction in the xz-plane.

To quantitatively assess the distribution of displacements to register XCT to CAD, in Fig. 7 we present a histogram showing the probability density function of the displacement along the three principal axes x, y and z. The histogram provides a statistical overview of the displacement distribution, revealing that displacement is particularly enhanced along the y-axis (corresponding to the building direction), as shown by the heatmap in Fig. 6.

The positive displacement along the y-axis suggests that the XCT volume was primarily undergoing shrinkage in this direction with respect to the CAD model during the AM process. The two main reasons of this behavior are that along the building direction the structure is less constrained, and that sagging is predominant in the vertical direction due to the effect of gravity. The notably greater shrinkage along the build axis is further motivated by early-stage shrinkage effects that occur before the PBF-LB process reaches steady-state, as reported in [31,32]. These initial shrinkage phenomena can substantially contribute to the overall deformation along the vertical direction, especially in small-scale components and when they are printed directly on the build plate without support structures.

Interestingly, while the heatmap in Fig. 6 also reveals a directional bias in the displacement within the xz-plane, the histogram in Fig. 7 does not exhibit a similar pattern. The mean displacement values along the x and z-axes are essentially zero. This discrepancy suggests that although there are directional biases visible in the heatmap, they may cancel out over the overall distribution, resulting in zero mean displacement along the x and z-axes.

5. Analysis of strain and mean displacement

Strain and displacement are key metrics to assess the deformation of a material during AM [33–36], though they quantify different aspects of the material's response to forces. While strain is a dimensionless measure reflecting relative changes in shape or size, displacement represents the absolute motion of a material point with units of length. In this study, both strain and displacement were computed directly from the displacement field using VTK. To fully characterize the deformation, we define the strain tensor $\boldsymbol{\epsilon}$ (see Eq. (4)), which captures both normal (diagonal) and shear (off-diagonal) strains.

$$\boldsymbol{\epsilon} = \begin{bmatrix} \epsilon_{xx} & \frac{1}{2}\gamma_{xy} & \frac{1}{2}\gamma_{xz} \\ \frac{1}{2}\gamma_{yx} & \epsilon_{yy} & \frac{1}{2}\gamma_{yz} \\ \frac{1}{2}\gamma_{zx} & \frac{1}{2}\gamma_{zy} & \epsilon_{zz} \end{bmatrix} \quad (4)$$

The components of the strain tensor at a specific vertex are derived from the vertex displacement vector $\mathbf{u}_i = (u_x^i, u_y^i, u_z^i)$ as follows. The normal strain quantifies the elongation or compression along a given axis and it is obtained as the derivative of the displacement vector components along the x, y, and z directions:

$$\epsilon_{xx}^i = \frac{\partial u_x^i}{\partial x}, \quad \epsilon_{yy}^i = \frac{\partial u_y^i}{\partial y}, \quad \epsilon_{zz}^i = \frac{\partial u_z^i}{\partial z} \quad (5)$$

To obtain a scalar measure of deformation, we computed the mean absolute normal strain over all deformed vertices in the mesh:

$$\bar{\epsilon}_{xx} = \frac{1}{N}\sum_{i=1}^{N} |\epsilon_{xx}^i|, \quad \bar{\epsilon}_{yy} = \frac{1}{N}\sum_{i=1}^{N} |\epsilon_{yy}^i|, \quad \bar{\epsilon}_{zz} = \frac{1}{N}\sum_{i=1}^{N} |\epsilon_{zz}^i| \quad (6)$$

where N is the total number of vertices. The shear strain describes angular distortion due to tangential forces and it is computed from the off-diagonal components of the displacement gradient:

$$\gamma_{xy}^i = \frac{\partial u_x^i}{\partial y} + \frac{\partial u_y^i}{\partial x}, \quad \gamma_{xz}^i = \frac{\partial u_x^i}{\partial z} + \frac{\partial u_z^i}{\partial x}, \quad \gamma_{yz}^i = \frac{\partial u_y^i}{\partial z} + \frac{\partial u_z^i}{\partial y} \quad (7)$$

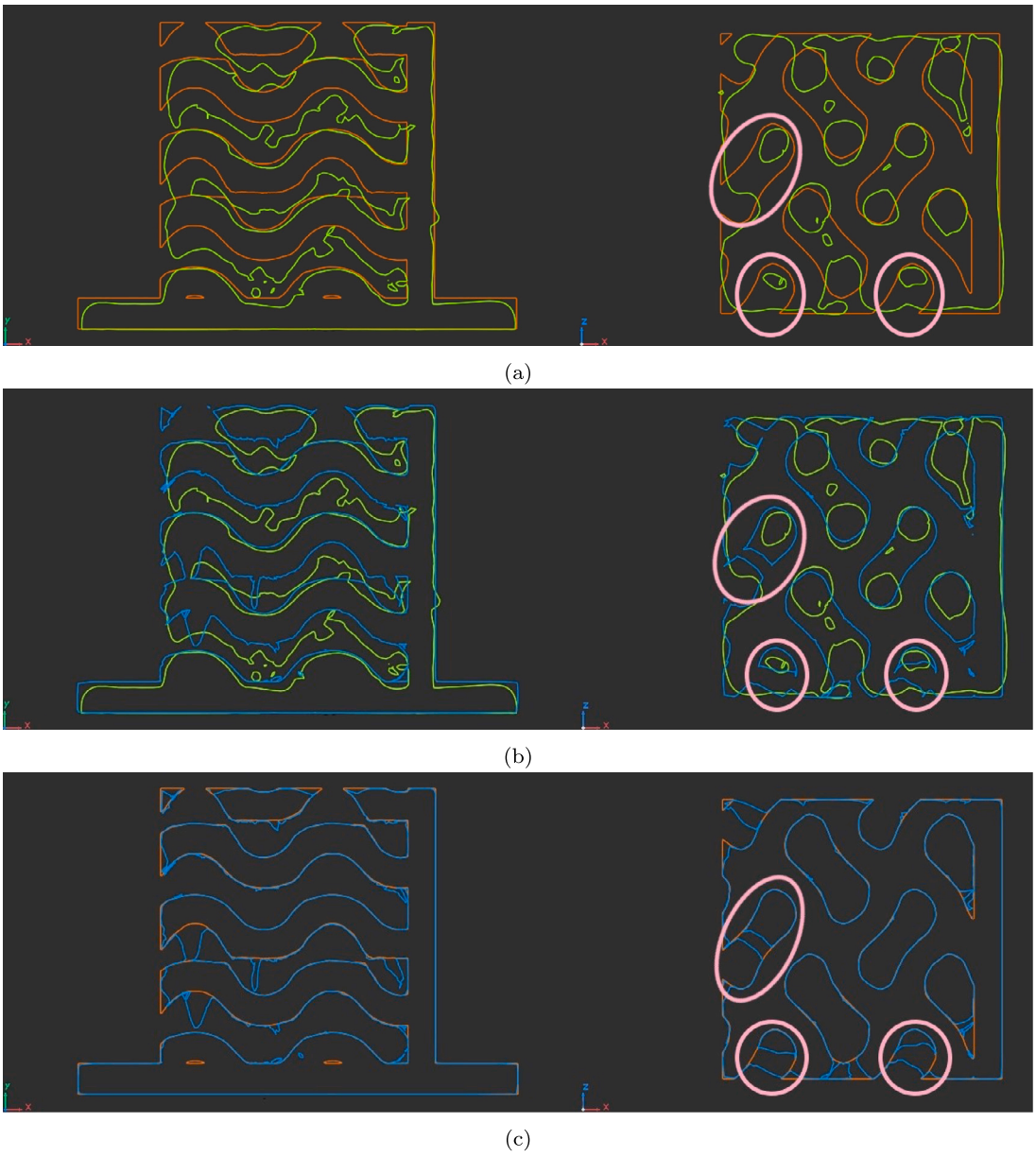

Fig. 4. Visualization of mesh alignment on 2D slices (on the left the xy-plane, on the right the xz-plane). (a) CAD model (orange) overlaid with the original XCT scan (green), (b) original XCT scan (green) overlaid with its non-linearly registered counterpart (blue), and (c) CAD model (orange) overlaid with the non-linearly registered XCT scan (blue). In the xz-plane on the right, we highlight with pink circles the areas where the registration fails due to severe splitting of the TPMS periodic voids into two components during the additive manufacturing process.

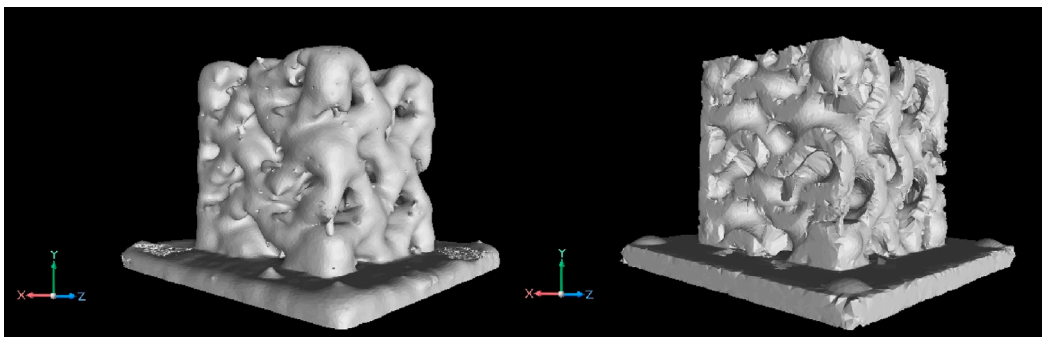

Fig. 5. Comparison of XCT before (left) and after (right) non-linear registration to the CAD model. The left side shows the raw linearly-registered XCT scan after smoothing, while the right side displays the smoothed XCT scan after non-linear registration.

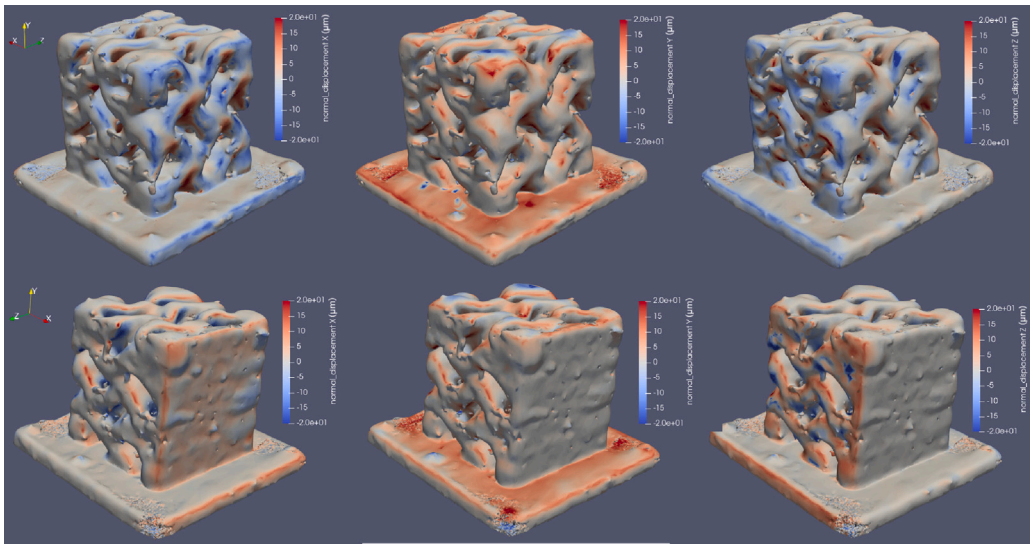

Fig. 6. Visualization of the normal displacement (μm) on the mesh vertices, when registering the XCT to the CAD. Warmer colors indicate larger outward (positive) displacements of the XCT mesh to align to the CAD mesh, while cooler colors indicate larger inward (negative) displacements of the XCT mesh to align to the CAD mesh. From left to right: x, y, and z components of the normal displacement.

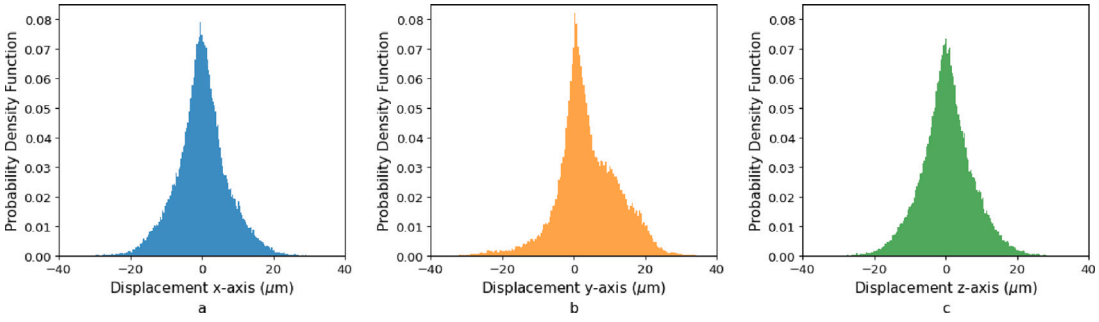

Fig. 7. Probability density function of displacement along x (a), y (b), and z (c) axes.

Again, we computed the mean absolute shear strain over all deformed vertices:

$$\bar{\gamma}_{xy} = \frac{1}{N}\sum_{i=1}^{N}|\gamma_{xy}^{i}|, \quad \bar{\gamma}_{xz} = \frac{1}{N}\sum_{i=1}^{N}|\gamma_{xz}^{i}|, \quad \bar{\gamma}_{yz} = \frac{1}{N}\sum_{i=1}^{N}|\gamma_{yz}^{i}| \tag{8}$$

On the other side, displacement quantifies the motion of a point in the material from its original position before registration. The mean displacement ($\bar{\mathbf{u}}$) is computed as:

$$\bar{\mathbf{u}} = \frac{1}{N}\sum_{i=1}^{N}\|\mathbf{u}_i\| \tag{9}$$

where $\mathbf{u}_i = (u_x^i, u_y^i, u_z^i)$ is the displacement vector at the ith vertex, $\|\mathbf{u}_i\|$ represents its magnitude, and N is the total number of deformed vertices in the mesh. To evaluate the displacement along each axis, we computed the mean absolute displacement in the x, y, and z directions:

$$\bar{u}_x = \frac{1}{N}\sum_{i=1}^{N}|u_x^i|, \quad \bar{u}_y = \frac{1}{N}\sum_{i=1}^{N}|u_y^i|, \quad \bar{u}_z = \frac{1}{N}\sum_{i=1}^{N}|u_z^i| \tag{10}$$

where $u_x^i = x_i' - x_i$, $u_y^i = y_i' - y_i$, and $u_z^i = z_i' - z_i$ represent the displacement components along the x, y, and z directions, respectively. Here, (x_i', y_i', z_i') are the coordinates of the deformed vertex after registration, and (x_i, y_i, z_i) are the original coordinates. In Fig. 8, we report the mean absolute displacement and mean absolute normal strain along the three principal axes (x, y, and z), as well as the mean absolute shear strain on the xy, yz, and xz-planes.

To assess the relevance of the mean absolute displacements within a volume of $125\,\text{mm}^3$, we compared these displacements to the characteristic dimension of the volume. Assuming an approximately cubic shape, the characteristic side length can be estimated as:

$$L \approx \sqrt[3]{125\,\text{mm}^3} = 5.00\,\text{mm} = 5000\,\mu\text{m}. \tag{11}$$

The relative displacements along the x, y, and z-axes were computed as:

$$\frac{\bar{u}_x}{L} = \frac{5.42\,\mu\text{m}}{5000\,\mu\text{m}} \approx 0.108\%, \tag{12}$$

$$\frac{\bar{u}_y}{L} = \frac{7.01\,\mu\text{m}}{5000\,\mu\text{m}} \approx 0.140\%, \tag{13}$$

$$\frac{\bar{u}_z}{L} = \frac{5.57\,\mu\text{m}}{5000\,\mu\text{m}} \approx 0.111\%. \tag{14}$$

These calculations indicate that the observed displacements along all three axes are below 0.15% of the characteristic length of the volume, making them relatively small in a macroscopic context. However, in high-precision applications, such as micromechanics or biotechnology, even micrometer-scale displacements can be significant.

While the mean displacement along the y-axis is the largest, as noted earlier in Section 4, the mean normal strain along the y-axis remains relatively close to those of the other two axes, at 0.51% compared to 0.50% and 0.52% along the x and z-axes, respectively. This indicates that although there was significant motion along the y-axis, the object deformed similarly in all directions. Furthermore, the mean shear strain along the three principal planes was computed and found to remain

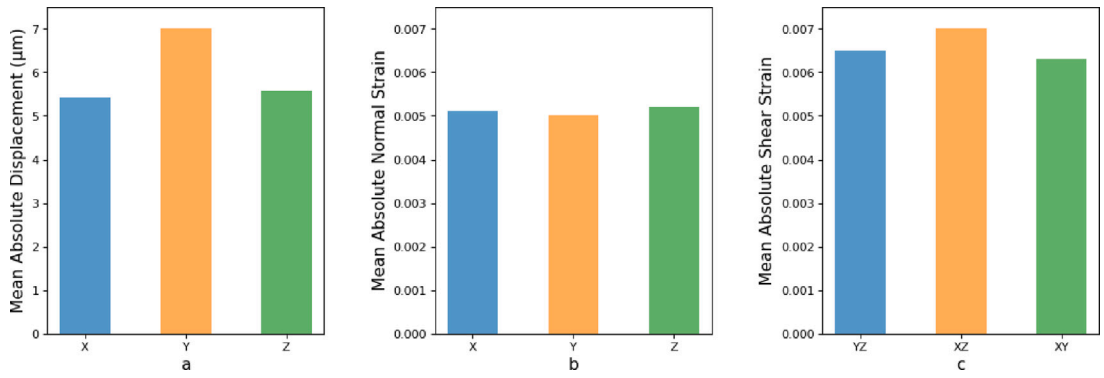

Fig. 8. Mean absolute displacement in μm (a) and mean absolute normal strain (adimensional) (b) along the three principal axes, as well as mean absolute shear strain (adimensional) (c) along the three different planes.

Table 1
Registration evaluation metrics comparing the registered XCT and CAD models before and after non-linear registration.

	TPMS structure
Linear registration	
Dice score	87.27%
MSE	7.24%
Non-linear registration	
Dice score	97.10%
MSE	1.95%

relatively low as well, with comparable values of 0.63%, 0.70%, and 0.65% for the xy, yz, and xz-planes, respectively.

6. Registration accuracy

To evaluate the registration accuracy between the CAD model and the registered XCT data, we computed the Dice score and the Mean Squared Error (MSE) on the segmented raw volumes. In order to do this, we converted the XCT registered mesh back to a binarized raw volume, i.e., we assigned the voxels as full (1 value) or empty (0 value) based on the registered mesh. This was done again with the advanced surface determination algorithm available in VGStudio Max software.

The Dice coefficient and MSE (see Eq. (15)) provide complementary perspectives on registration accuracy. The Dice score is a widely used metric in image segmentation [37–40], which rewards correctly segmented voxels and penalizes incorrect ones. On the other side, the MSE simply quantifies the absolute voxel-wise intensity differences.

$$\text{Dice Score} = \frac{2TP}{2TP + FP + FN} \qquad \text{MSE} = \frac{1}{N}\sum_{i=1}^{N}(X_i - Y_i)^2 \tag{15}$$

Here TP, FP, and FN indicate True-Positive, False-Positive, and False-Negative voxels; it is important to note that TP voxels correspond to regions where the registered XCT and the CAD align perfectly. On the other hand, X_i and Y_i directly represent voxel intensities (in our case either 0 or 1) for the registered XCT and CAD volumes respectively, and N is the total number of voxels.

Table 1 presents the quantitative comparison between linear and non-linear registration. The Dice score reflects a high degree of overlap between the registered XCT and CAD models, with non-linear registration significantly improving accuracy. Indeed, the Dice score for the TPMS structure increased from 87.27% to 97.10% after non-linear registration. Similarly, the MSE sees a substantial improvement as well, with a reduction from 7.24% to 1.95%, confirming that the non-linear registration was successful. These results highlight the effectiveness of the non-linear registration pipeline in achieving higher structural fidelity and minimizing misalignment when compared to linear registration.

7. Conclusion

With the aim of determining dimensional distortions of additively manufactured parts (in our case PBF-LB-AlSi10Mg lattice structure) after printing, we used the Chamfer distance loss to evaluate and refine mesh non-linear deformations on complex Triply Periodic Minimal Surface lattices. We started from X-ray Computed Tomography 3D reconstructions, we meshed them and we registered them to the CAD model (used as input for the AM process). Our results demonstrate that Chamfer Distance is highly effective in capturing geometric discrepancies and describing the deformation process. In fact, our method uses a non-linear registration, thereby capturing fine details of the distortion field. The advantages of the Chamfer method, with respect for instance to deep learning approaches, are its simplicity, speed, and transparency. We estimated the errors and evaluated the accuracy of the registration by the Dice Score and the Mean Square Error. Furthermore, we analyzed the strain and displacement from the displacement field associated to the registration transformation and we found that the volume is primarily shrinking along the building direction during the AM process.

CRediT authorship contribution statement

Michela Lapenna: Writing – original draft, Methodology, Investigation, Formal analysis, Data curation, Conceptualization. **Francesco Faglioni:** Writing – review & editing, Supervision, Methodology, Investigation, Formal analysis, Conceptualization. **Keerthana Chand:** Writing – review & editing, Methodology, Data curation. **Bardia Hejazi:** Writing – review & editing, Data curation. **Rita Fioresi:** Writing – review & editing, Supervision. **Giovanni Bruno:** Writing – review & editing, Supervision.

Declaration of competing interest

The authors declare that no conflict of interest may have influenced the work in this paper.

Acknowledgments

We thank Domenico Iuso and Tobias Fritsch for their valuable suggestions, and Tobias Fritsch specifically for acquiring the TPMS XCT scans at BAM.

This research was funded by CaLISTA CA 21109; CaLIGOLA MSCA-2021-SE-01-101086123; MSCA-DN CaLiForNIA—101119552; PNRR MNESYS; the PNRR National Center for HPC, Big Data, and Quantum Computing; SimQuSec; INFN Sezione Bologna; Gast initiative and GNSAGA Indam. Funding for ML from BAM Project QI Digital is acknowledged. FF acknowledges UNIMORE FAR-DIP DSCG 2023.

Data availability

Data will be made available on request.

References

[1] K. Chand, T. Fritsch, S. Oster, A. Ulbricht, G. Bruno, Review on image registration methods for the quality control in additive manufacturing, Prog. Addit. Manuf. (2025) 1–27, http://dx.doi.org/10.1007/s40964-024-00932-2.

[2] S.C. Feng, Y. Lu, A.T. Jones, Z. Yang, Additive manufacturing in situ and ex situ geometric data registration, J. Comput. Inf. Sci. Eng. 22 (6) (2022) 061003, http://dx.doi.org/10.1115/1.4054202.

[3] A. Lang, C.O. Rios, J.W. Newkirk, R.G. Landers, J. Castle, D.A. Bristow, Image registration and matching error in 2d and 3d for laser powder bed fusion, 2021, URL https://api.semanticscholar.org/CorpusID:245352279.

[4] B.M. Colosimo, M. Grasso, F. Garghetti, B. R, Complex geometries in additive manufacturing: A new solution for lattice structure modeling and monitoring, J. Qual. Technol. 54 (4) (2022) 392–414, http://dx.doi.org/10.1080/00224065.2021.1926377, arXiv:https://doi.org/10.1080/00224065.2021.1926377.

[5] VoxelMorph, A learning framework for deformable medical image registration, IEEE Trans. Med. Imaging (2019) URL https://github.com/voxelmorph/voxelmorph.

[6] Z. Wang, H. Delingette, Attention for image registration (air): an unsupervised transformer approach, 2021, ArXiv abs/2105.02282 URL https://api.semanticscholar.org/CorpusID:233864961.

[7] M. Meng, L. Bi, D. Feng, J. Kim, Non-iterative coarse-to-fine registration based on single-pass deep cumulative learning, Med. Image Comput. Comput. Assist. Interv. – MICCAI 2022 (2022) 88–97.

[8] R. Jena, P. Chaudhari, J.C. Gee, Deep implicit optimization enables robust learnable features for deformable image registration, 2024, arXiv:2406.07361 URL https://arxiv.org/abs/2406.07361.

[9] H.G. Barrow, J.M. Tenenbaum, R.C. Bolles, H.C. Wolf, Parametric correspondence and chamfer matching: Two new techniques for image matching, in: International Joint Conference on Artificial Intelligence, 1977, URL https://api.semanticscholar.org/CorpusID:1621080.

[10] M. Zhao, G. Meng, D.-M. Yan, Occlusion-aware non-rigid point cloud registration via unsupervised neural deformation correntropy, 2025, arXiv:2502.10704 URL https://arxiv.org/abs/2502.10704.

[11] H. Fan, H. Su, L. Guibas, A point set generation network for 3d object reconstruction from a single image, in: 2017 IEEE Conference on Computer Vision and Pattern Recognition, CVPR, IEEE Computer Society, Los Alamitos, CA, USA, 2017, pp. 2463–2471, http://dx.doi.org/10.1109/CVPR.2017.264, URL https://doi.ieeecomputersociety.org/10.1109/CVPR.2017.264.

[12] X. Li, J.K. Pontes, S. Lucey, Neural scene flow prior, in: Proceedings of the 35th International Conference on Neural Information Processing Systems, NIPS '21, Curran Associates Inc. Red Hook, NY, USA, 2021.

[13] Y. Li, T. Harada, Non-rigid point cloud registration with neural deformation pyramid, in: Proceedings of the 36th International Conference on Neural Information Processing Systems, NIPS '22, Curran Associates Inc. Red Hook, NY, USA, 2022.

[14] S. Prokudin, Q. Ma, M. Raafat, J. Valentin, S. Tang, Dynamic point fields, in: Proceedings of the IEEE/CVF International Conference on Computer Vision, ICCV, 2023, pp. 7964–7976.

[15] F.L. Bookstein, Principal warps: Thin-plate splines and the decomposition of deformations, IEEE Trans. Pattern Anal. Mach. Intell. 11 (6) (1992) 567–585, http://dx.doi.org/10.1109/34.100305.

[16] D. Rueckert, L.I. Sonoda, C. Hayes, D.L.G. Hill, M.O. Leach, D.J. Hawkes, Nonrigid registration using free-form deformations: Application to breast mr images, IEEE Trans. Med. Imaging 18 (8) (2003) 712–721, http://dx.doi.org/10.1109/42.796284.

[17] J. Feng, J. Fu, X. Yao, Y. He, Triply periodic minimal surface (tpms) porous structures: from multi-scale design, precise additive manufacturing to multi-disciplinary applications, Int. J. Extrem. Manuf. 4 (2022) URL https://api.semanticscholar.org/CorpusID:247372643.

[18] I. Maskery, N. Aboulkhair, A. Aremu, C. Tuck, I. Ashcroft, R. Wildman, R. Hague, A mechanical property evaluation of graded density al-si10-mg lattice structures manufactured by selective laser melting, Mater. Sci. Eng.: A 670 (2016) 264–274, http://dx.doi.org/10.1016/j.msea.2016.06.013.

[19] L. Yang, O. Harrysson, H. West, D. Cormier, Compressive properties of ti-6al-4v auxiliary mesh structures for energy absorption applications, Addit. Manuf. 27 (2019) 53–63, http://dx.doi.org/10.1016/j.addma.2019.02.002.

[20] O. Al-Ketan, R. Rowshan, R. Abu Al-Rub, Topology-mechanical property relationship of 3d printed strut, skeletal, and sheet-based periodic metallic cellular materials, Addit. Manuf. 36 (2020) 101405, http://dx.doi.org/10.1016/j.addma.2020.101405.

[21] Xunjin Li, Peng Qu, He Kong, Yonghao Lei, Anfu Guo, Shaoqing Wang, Yi Wan, Jun Takahashi, Enhanced mechanical properties of sandwich panels via integrated 3D printing of continuous fiber face sheet and TPMS core, Thin-Walled Struct. 204 (2024) 112312, http://dx.doi.org/10.1016/j.tws.2024.112312.

[22] O. Al-Ketan, R. Rezgui, R. Rowshan, H.F. Du, N.X. Fang, R.K. Abu Al-Rub, Microarchitected stretching-dominated mechanical metamaterials with minimal surface topologies, Adv. Eng. Mater. 20 (9) (2018) 1800029, http://dx.doi.org/10.1002/adem.201800029.

[23] E.A.R. Salazar, Design of Functionally Graded Parts for Additive Manufacturing: Methods and Tools for Variable Density Triply Periodic Minimal Surfaces, (Ph.D. thesis), Université Grenoble Alpes, 2022.

[24] M. Luethi, B. Bircher, F. Meli, A. Küng, R. Thalmann, X-ray flat-panel detector geometry correction to improve dimensional computed tomography measurements, Meas. Sci. Technol. 31 (2019) http://dx.doi.org/10.1088/1361-6501/ab52b1.

[25] K. Chand, T. Fritsch, S. Oster, A. Ulbricht, K. Poka, G. Bruno, A comparative study of rigid three-dimensional image registration methods for powder bed fusion with laser beam of metals using a gold standard approach, J. Nondestruct. Eval. 44 (1) (2025) 30, http://dx.doi.org/10.1007/s10921-025-01174-0.

[26] Z. Niu, H. Suzuki, Y. Ohtake, T. Michikawa, Mesh generation of porous metals from x-ray computed tomography volume data, J. Mech. Sci. Technol. 28 (2013) 2445–2451, URL https://api.semanticscholar.org/CorpusID:111121715.

[27] C. Koc, O. Pinarer, S. Turhan, 3D mesh model generation from ct and mri data, in: 2021 IEEE International Conference on Big Data (Big Data), 2022, pp. 4725–4730.

[28] X. Zheng, G. Xu, 3D finite element meshing from imaging data, in: Proceedings of the 2009 International Conference on Image Processing, Computer Vision, and Pattern Recognition, 2009, pp. 1–6.

[29] S. Ruder, An overview of gradient descent optimization algorithms, 2016, ArXiv abs/1609.04747 URL https://api.semanticscholar.org/CorpusID:17485266.

[30] Facebook AI Research, Deform a source mesh to form a target mesh using 3d loss functions, 2020, https://pytorch3d.org/tutorials/deform_source_mesh_to_target_mesh.

[31] F. Zanini, N. Bonato, S. Carmignato, New multi-function building plate for improving metal laser powder bed fusion by enhancing the alignment accuracy of in-process monitoring data, computed tomography measurements, and building volume geometry, Int. J. Adv. Manuf. Technol. 132 (2024) http://dx.doi.org/10.1007/s00170-024-13514-x.

[32] F. Zanini, N. Bonato, S. Carmignato, New experimental approach for local measurements of effective layer thickness, powder bed density and volumetric energy density to enhance metal laser powder bed fusion, Addit. Manuf. 93 (2025) http://dx.doi.org/10.1016/j.addma.2024.104432.

[33] N. Bastola, M.P. Jahan, N. Rangasamy, C.S. Rakurty, A review of the residual stress generation in metal additive manufacturing: Analysis of cause, measurement, effects, and prevention, Micromachines 14 (7) (2023) http://dx.doi.org/10.3390/mi14071480, URL https://www.mdpi.com/2072-666X/14/7/1480.

[34] W. Dong, X. Liang, Q. Chen, S. Hinnebusch, Z. Zhou, A.C. To, A new procedure for implementing the modified inherent strain method with improved accuracy in predicting both residual stress and deformation for laser powder bed fusion, Addit. Manuf. 47 (C) (2021) http://dx.doi.org/10.1016/j.addma.2021.102345.

[35] P. Pourabdollah, F.F. Mehr, S. Cockcroft, D.M. Maijer, A new variant of the inherent strain method for the prediction of distortion in powder bed fusion additive manufacturing processes, Int. J. Adv. Manuf. Technol. 131 (2024) 4575–4594, URL https://api.semanticscholar.org/CorpusID:268180452.

[36] Xunjin Li, Peng Qu, He Kong, Yingdan Zhu, Cong Hua, Anfu Guo, Shaoqing Wang, Multi-scale numerical analysis of damage modes in 3D stitched composites, Int. J. Mech. Sci. 266 (2024) 108983, http://dx.doi.org/10.1016/j.ijmecsci.2024.108983.

[37] T. Strohmann, K. Bugelnig, E. Breitbarth, F. Wilde, T. Steffens, H. Germann, G. Requena, Semantic segmentation of synchrotron tomography of multiphase al-si alloys using a convolutional neural network with a pixel-wise weighted loss function, Sci. Rep. (2019) http://dx.doi.org/10.1038/s41598-019-56008-7.

[38] A. Tsamos, S. Evsevleev, R. Fioresi, F. Faglioni, G. Bruno, Synthetic data generation for automatic segmentation of x-ray computed tomography reconstructions of complex microstructures, J. Imaging 9 (2) (2023) http://dx.doi.org/10.3390/jimaging9020022.

[39] M. Lapenna, A. Tsamos, F. Faglioni, R. Fioresi, F. Zanchetta, G. Bruno, Geometric deep learning for enhanced quantitative analysis of microstructures in x-ray computed tomography data, Discov. Appl. Sci. 6 (2024) http://dx.doi.org/10.1007/s42452-024-05985-0.

[40] M. Lapenna, A. Tsamos, F. Faglioni, R. Fioresi, F. Zanchetta, G. Bruno, Vision GNN (ViG) architecture for a fine-tuned segmentation of a complex al–si metal matrix composite XCT volume, J. Mater. Sci. 60 (16) (2025) 6907–6921, http://dx.doi.org/10.1007/s10853-025-10834-5.